Editors' Suggestion | Featured in Physics

Scalable Multipartite Entanglement Created by Spin Exchange in an Optical Lattice

Wei-Yong Zhang,[1,2,*] Ming-Gen He,[1,2,*] Hui Sun,[1,2,*] Yong-Guang Zheng,[1,2] Ying Liu,[1,2] An Luo,[1,2] Han-Yi Wang,[1,2] Zi-Hang Zhu,[1,2] Pei-Yue Qiu,[1,2] Ying-Chao Shen,[1,2] Xuan-Kai Wang,[1,2] Wan Lin,[1,2] Song-Tao Yu,[1,2] Bin-Chen Li,[1,2] Bo Xiao,[1,2] Meng-Da Li,[1,2] Yu-Meng Yang,[1,2] Xiao Jiang,[1,2] Han-Ning Dai,[1,2] You Zhou,[1,3] Xiongfeng Ma,[4] Zhen-Sheng Yuan,[1,2,5] and Jian-Wei Pan[1,2,5]

[1]*Hefei National Research Center for Physical Sciences at the Microscale and School of Physical Sciences, University of Science and Technology of China, Hefei 230026, China*

[2]*CAS Center for Excellence in Quantum Information and Quantum Physics, University of Science and Technology of China, Hefei 230026, China*

[3]*Key Laboratory for Information Science of Electromagnetic Waves (Ministry of Education), Fudan University, Shanghai 200433, China*

[4]*Center for Quantum Information, Institute for Interdisciplinary Information Sciences, Tsinghua University, Beijing 100084, China*

[5]*Hefei National Laboratory, University of Science and Technology of China, Hefei 230088, China*

(Received 25 April 2023; accepted 30 June 2023; published 18 August 2023)

Ultracold atoms in optical lattices form a competitive candidate for quantum computation owing to the excellent coherence properties, the highly parallel operations over spins, and the ultralow entropy achieved in qubit arrays. For this, a massive number of parallel entangled atom pairs have been realized in superlattices. However, the more formidable challenge is to scale up and detect multipartite entanglement, the basic resource for quantum computation, due to the lack of manipulations over local atomic spins in retroreflected bichromatic superlattices. In this Letter, we realize the functional building blocks in quantum-gate-based architecture by developing a cross-angle spin-dependent optical superlattice for implementing layers of quantum gates over moderately separated atoms incorporated with a quantum gas microscope for single-atom manipulation and detection. Bell states with a fidelity of 95.6(5)% and a lifetime of 2.20 ± 0.13 s are prepared in parallel, and then connected to multipartite entangled states of one-dimensional ten-atom chains and two-dimensional plaquettes of 2×4 atoms. The multipartite entanglement is further verified with *full bipartite nonseparability* criteria. This offers a new platform toward scalable quantum computation and simulation.

DOI: 10.1103/PhysRevLett.131.073401

Introduction.—Entanglement is the key resource for applications in quantum information science [1–4]. To achieve the long-term pursuit to realize scalable multipartite entanglement, remarkable advances have been made in different quantum platforms including photons, superconducting circuits, trapped ions, and neutral atoms in tweezer arrays [5–13]. An alternative system, ultracold atoms in optical lattices, can promisingly enable a programmable approach to generate scalable two-dimensional (2D) entanglement thanks to a large number of atomic qubits generated through a quantum phase transition and highly parallel spin operations [14–19]. Recently, progress has been achieved in manipulating atomic qubits in optical lattices [20–25]. These advances support a prospective scheme to scale up multipartite entanglement with quantum gates provided by controllable bichromatic superlattices [4], where the landmarks include generating isolated entangled Bell pairs in parallel, entangling Bell pairs into one-dimensional (1D) chains, and further realizing 2D entangled plaquettes. As a first step, the parallel preparation of isolated Bell pairs has been demonstrated with quantum gates in tunable superlattices [19,21].

The next critical step is to realize the cascade of entangling gates applied on configurable qubit arrays along the two spatial dimensions, leading to the programmable generation of 2D multipartite spin entanglement. This approach requires the combination of all the fundamental operations, including local spin manipulation, parallel controllable entangling gates, and single-site-resolved detection of spin states. However, the small atom separation in conventional retroreflected bichromatic superlattices [26] is beyond the current imaging resolution in systems of neutral alkali atoms [23,24]. In addition, the accumulating noise of the quantum gates and the decoherence of the qubits can degrade the final multipartite entanglement, limiting the effectiveness of quantum circuits in optical lattices.

In this Letter, we demonstrate the functional building blocks for generating and probing scalable multipartite atomic entanglement in optical lattices. This is realized by

developing a cross-angle spin-dependent optical superlattice for trapping moderately separated atoms incorporated with a quantum gas microscope for single-atom manipulation. Parallel and local spin controllability is developed by combining the spin-dependent superlattice and versatile atom addressing techniques in the single-site precision using digital micromirror devices (DMDs) [27,28]. Actively reducing the noise of magnetic fields and lasers, long-lived Bell pairs with a lifetime of 2.20 ± 0.13 s are prepared using parallel high-fidelity entangling gates based on the superexchange effect in double wells. We then demonstrate the programmable generation of 1D and 2D multipartite entangled states by entangling a ten-atom chain and a plaquette of 2×4 atoms. The *full bipartite nonseparability* of these states is experimentally verified with the site- and spin-resolved detection methods.

Preparing a defect-free 2D qubit array.—In the experiment, ultracold ^{87}Rb atoms are loaded into a 2D far-detuned optical superlattice generated by equal-arm interferometers, which are constructed by 532-nm/1064-nm lasers for short/long lattices along both the x and y direction [28,33]. The lattice spacing is 630 nm resulting from the cross angle of 50 degrees between the short lattices, well resolved with our imaging resolution. This equal-arm configuration is resistant to external perturbations and leads to the long-term stability of the absolute location of the lattice sites. By tuning the spin dependency and relative phases of the superlattice, the experimental setup is further equipped with the parallel and local manipulation over atomic spin states and the single-site-resolved detection, which enable parallel assembly of large-scale defect-free qubits with the recently demonstrated cooling method [21]. In addition, we apply a repulsive optical potential projected by a DMD to compensate for the harmonic confinement originating from the Gaussian envelope of lattice beams.

Figure 1(b) shows an exemplary fluorescence image of the atomic distribution after removing the superfluid reservoirs and the marked region of interest (ROI) containing 18×14 lattice sites. Considering the detection loss during imaging, the overall fidelity for preparing a unity filling state across 200 lattice sites is 99.2(2)% [the value in parentheses represents standard error of the mean (s.e.m.)] [28], obtained from around 400 experimental repetitions. The hyperfine ground states $|\downarrow\rangle = |F = 1, m_F = -1\rangle$ and $|\uparrow\rangle = |F = 2, m_F = -2\rangle$ are used to encode the qubit states. The atoms possess excellent single-qubit coherence, as verified by driven Rabi oscillations accompanied by an exponential decay with a time constant of $\tau_{\mathrm{Rabi}} = 42.9 \pm 7.0$ ms in Fig. 1(e).

Site- and spin-resolved state photography and entangled pairs.—With the defect-free qubit array, the entangling $\sqrt{\mathrm{SWAP}}^{\dagger}$ gate based on the spin superexchange interaction

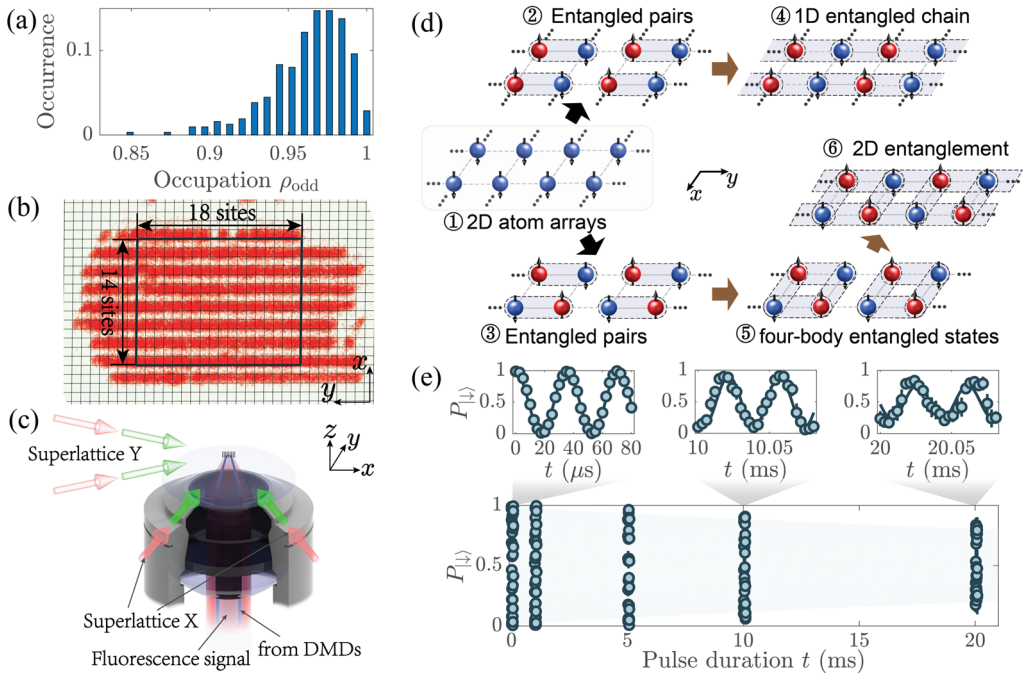

FIG. 1. Experimental setup and entanglement generation sketch. (a) Bar chart of the average occupation in the ROI as indicated in (b) after cooling atoms in the superlattice. (b) An exemplary fluorescence image of the atom array after cooling, with the marked ROI containing 18×14 lattice sites. (c) Simplified setups for cooling, entangling, and detecting the atoms in optical lattices (for details, refer to the Supplemental Material [28]). (d) Cartoon schematic of generating multipartite entanglement in optical lattices by parallel cascading the entangling gates to prepare isolated Bell pairs ① → ②/③ and further connecting them to realize 1D entangled chains ② → ④ and 2D entangled plaquettes ③ → ⑤ → ⑥. (e) Measured occupation of the $|\downarrow\rangle$ state in the driven Rabi oscillation via the Stern-Gerlach-type approach [28], indicating an exponential decay with a time constant of $\tau_{\mathrm{Rabi}} = 42.9 \pm 7.0$ ms.

is investigated in a site-resolved way within a smaller ROI containing 14×14 lattice sites. The experiment starts by first preparing the two ^{87}Rb atoms in each isolated double-well in a Néel-type antiferromagnetic order $|\uparrow,\downarrow\rangle$ (the comma separating the left and right occupations). With the auxiliary unoccupied lattice sites alternately arranged along the x direction, we can apply a Stern-Gerlach-type single-spin-resolved detection [28] to directly visualize the dynamic evolution of these four spin states, $\{|\uparrow,\downarrow\rangle, |\downarrow,\uparrow\rangle, |\uparrow\downarrow,0\rangle, |0,\uparrow\downarrow\rangle\}$ [34].

Figure 2(a) shows the measured time-resolved average occupancy $\rho_{|\uparrow,\downarrow\rangle}$ of the $|\uparrow,\downarrow\rangle$ state over the 49 double wells, which reveals the expected sinusoidal oscillation at a frequency of $J_{\mathrm{ex}}/h = 20.5 \pm 0.1$ Hz. The residual inhomogeneity of trapping potential induces a slight deviation in the synchronization in different double wells (as shown in Fig. S8 in the Supplemental Material [28]) during the evolution.

We then prepare two-atom entangled Bell states in parallel using entangling gates $\sqrt{\mathrm{SWAP}}^{\dagger}$. This is realized by halting the superexchange dynamics at a fixed evolution time of $t = 5.6$ ms, followed by a phase rotation [35]. From the measured two-atom spin correlations shown in Fig. 2(c), we characterize the average fidelity of Bell states in the ROI as $\mathcal{F} = 0.956 \pm 0.005$ [28]. The coherence time of the Bell states is obtained by the Ramsey interference measurement, implemented with the singlet-triplet oscillation after variable holding time. As shown in Fig. 2(d), the extracted oscillation amplitudes exhibit the exponential decay with a time constant of $\tau = 2.20 \pm 0.13$ s [36–38].

Connecting entangled pairs to 1D and 2D multipartite entanglement.—We next demonstrate the generation of 1D entanglement by cascading two parallel layers of entangling gates. The initial state is prepared as a chain of 10 qubits with the Néel-order magnetization, where all other atoms in the array are removed by applying the site-resolved atom addressing techniques. Shown in Fig. 3(a), after preparing isolated two-atom entangled Bell states, we change the relative phase θ_y of the superlattice to form new atom pairs and then apply another parallel layer of $\sqrt{\mathrm{SWAP}}^{\dagger}$ gates. Since verifying that the ten-atom state is *genuine multipartite entanglement* requires a rather complicated measurement procedure, we develop an efficient entanglement criterion based on the scheme [39], which can verify that the prepared state possesses *full bipartite nonseparability*, i.e., the state is inseparable with respect to any fixed partition [28,39].

According to the new criterion, we only need to measure the final spin configuration under two settings of bases, $\sigma_x^{\otimes 10}$ and $\sigma_z^{\otimes 10}$, given by whether to apply a global $\pi/2$ rotation pulse before the projection measurement. The measurement results of two-particle spin correlations are shown in Figs. 3(c) and 3(d). All the observables $\gamma_{i,j} = 2|\langle\sigma_x^i\sigma_x^j\rangle| + |\langle\otimes_{k=1}^{10}\sigma_z^k\rangle|$, shown in Fig. 3(e), surpass the threshold, verifying that the ten-atom chain cannot be divided into any two separated partitions.

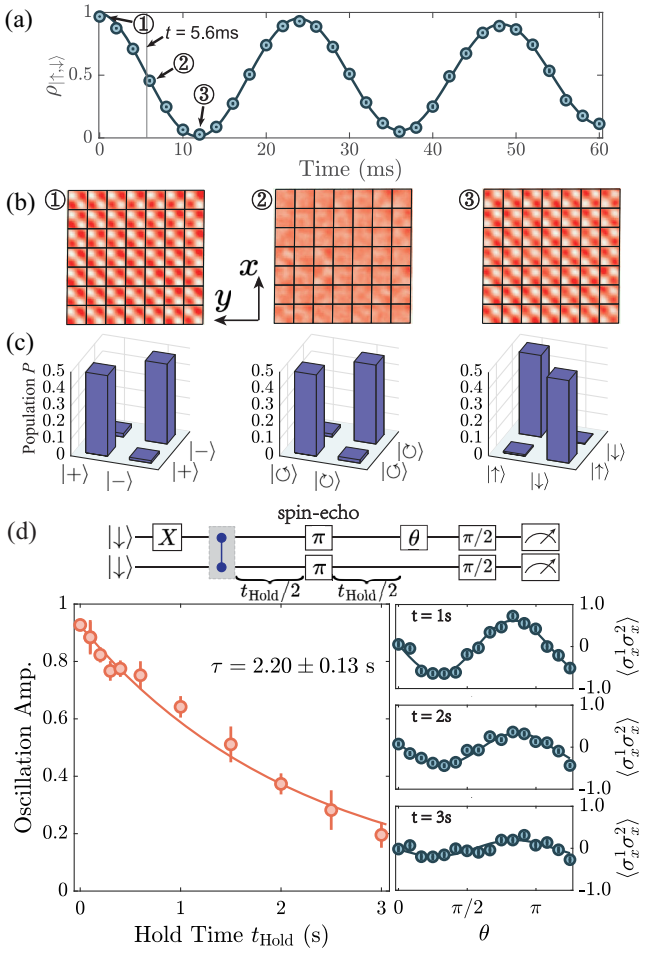

FIG. 2. Superexchange dynamics and Bell states. (a) The averaged occupancy $\rho_{|\uparrow,\downarrow\rangle}$ (circles) of the $|\uparrow,\downarrow\rangle$ state, showing the superexchange dynamics in isolated double wells within the ROI. The fitted curve (solid line) with a damped sinusoidal function gives the averaged exchange strength $J_{\mathrm{ex}} = 20.5 \pm 0.1$ Hz. (b) The averaged spin configurations were measured in the 49 plaquettes during the spin superexchange process in double wells. (c) Measured populations under $|+/-\rangle$, $|\circlearrowleft/\circlearrowright\rangle$, and $|\uparrow/\downarrow\rangle$ basis for the prepared Bell states averaged within the ROI gives $P_{+,+} = 0.484 \pm 0.007$, $P_{+,-} = 0.021 \pm 0.003$, $P_{-,+} = 0.015 \pm 0.002$, $P_{-,-} = 0.480 \pm 0.007$, $P_{\circlearrowleft,\circlearrowleft} = 0.488 \pm 0.010$, $P_{\circlearrowleft,\circlearrowright} = 0.018 \pm 0.002$, $P_{\circlearrowright,\circlearrowleft} = 0.020 \pm 0.003$, $P_{\circlearrowright,\circlearrowright} = 0.474 \pm 0.008$, $P_{\uparrow,\uparrow} = 0.010 \pm 0.001$, $P_{\uparrow,\downarrow} = 0.490 \pm 0.009$, $P_{\downarrow,\uparrow} = 0.496 \pm 0.009$, $P_{\downarrow,\downarrow} = 0.004 \pm 0.001$. (d) The extracted parity oscillation contrast of the prepared Bell states after different holding times with a spin-echo π pulse, fitted as an exponential decay with a time constant $\tau = 2.20 \pm 0.13$ s. Error bars denote the s.e.m.

Next, we demonstrate the 2D gate-based quantum circuit of generating and measuring entangled states of four atoms in a 2×2 plaquette and eight atoms in a 2×4 plaquette, respectively.

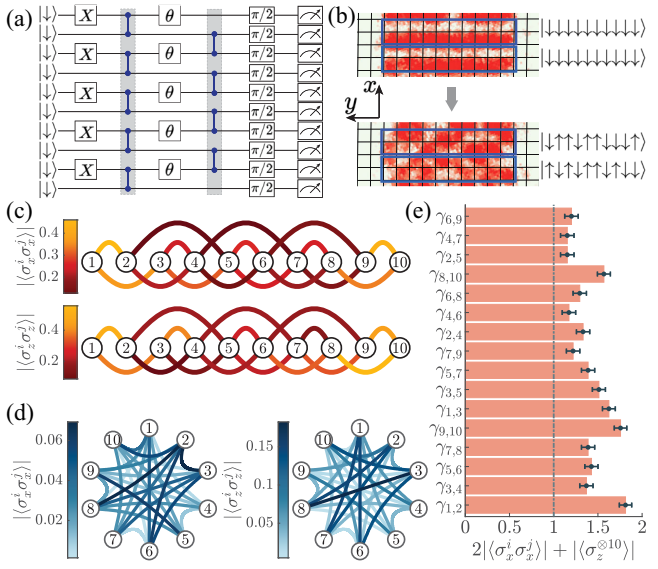

FIG. 3. Ten-body entangled state. (a) Quantum circuit representation for preparing and measuring a ten-body entangled state. (b) Exemplary fluorescence images of the initial atom arrays (upper panel) and the prepared ten-atom entangled state (lower panel), detected with the Stern-Gerlach type measurement [28]. (c) For the target entangled state, theoretical values of these two-body correlations under the σ_x and σ_z basis are nonzero. (d) The theoretical values of these two-body correlations under the σ_x and σ_z basis are all zero for the target state. (e) The extracted results of observables $\gamma_{i,j}$. The dashed-dot line represents the threshold for verifying *full bipartite nonseparability*. Since $\gamma_{1,2} = 1.81 \pm 0.09$, $\gamma_{3,4} = 1.37 \pm 0.10$, $\gamma_{5,6} = 1.43 \pm 0.10$, $\gamma_{7,8} = 1.39 \pm 0.10$, and $\gamma_{9,10} = 1.76 \pm 0.09$, we conclude that atoms 1 and 2, 3 and 4, 5 and 6, 7 and 8, and 9 and 10 are nonseparable, respectively. Moreover, since $\gamma_{1,3} = 1.62 \pm 0.10$, $\gamma_{3,5} = 1.51 \pm 0.10$, $\gamma_{5,7} = 1.39 \pm 0.10$, and $\gamma_{8,10} = 1.57 \pm 0.10$, we deduce that the ten-atom chain cannot be divided into any two separated partitions [28]. Error bars denote the s.e.m.

Since the Stern-Gerlach techniques are no longer applicable for measuring 2D entanglement, we develop a new detection approach to resolve the atomic spins on each site using state-dependent atom transport. As illustrated in Fig. 4(a), we first shine a state-dependent addressing beam shaped by a DMD to pin the $|\uparrow\rangle$ atoms and then change the phase of the long lattice to transport the $|\downarrow\rangle$ atoms to the originally unoccupied auxiliary sites before performing fluorescence imaging. Atoms in the two spin states can be distinguished simultaneously by their final positions. The average fidelity of this detection technique is around 98.5% (as shown in Table E.1 in the Supplemental Material [28]), where the inefficiency is attributed to the influence of crosstalking between different spin states and accidental atom hopping during the detection.

Figure 4(b) shows the preparation of four-body entanglement in isolated 2×2 plaquettes. We begin with a 2D Néel-order magnetization. After the first parallel layer of $\sqrt{\text{SWAP}}^\dagger$ gates generate Bell pairs along the y direction, we realize the four-body entangled state by applying a second layer of $\sqrt{\text{SWAP}}^\dagger$ gates along the x direction. The target state is a stabilizer state [28]. The generators of its stabilizer group are $\sigma_z^1\sigma_z^2$, $\sigma_z^3\sigma_z^4$, $\sigma_z^1\sigma_x^3\sigma_x^4$ and $-\sigma_x^1\sigma_x^2\sigma_z^3$. To characterize this state, the spin correlations extracted from the two measurement settings, $\sigma_x^1\sigma_x^2\sigma_z^3\sigma_z^4$ and $\sigma_z^1\sigma_z^2\sigma_x^3\sigma_x^4$, are obtained by performing projective measurements after a local $\pi/2$ pulse is applied to two bottom sites or the two top sites [28]. The measured expectation values, as shown in Fig. 4(b), satisfy the inequality Eq. (G.12) in the Supplemental Material [28], thus verifying the four-body state is *genuine multipartite entanglement*.

Furthermore, we realize the 2D eight-body entanglement in the 2×4 plaquette by applying one more layer of entangling gates to connect neighboring 2×2 plaquettes, as shown in Fig. 4(c). After entangling atoms in an isolated 2×2 plaquette as above, we switch the relative phase θ_y of the superlattice along the y direction and further apply another layer of parallel $\sqrt{\text{SWAP}}^\dagger$ gates to entangle these adjacent plaquettes. With the following steps, we characterize this state by verifying the *full bipartite nonseparability*. First, we perform the same measurements as above to demonstrate a four-body entangled state in isolated plaquettes. Shown in Fig. 4(d), the yielded observables surpass the threshold, certifying the *full bipartite nonseparability* property inside the two separate chains along the y direction. Then, we demonstrate *full bipartite nonseparability* property between these two chains. To build proper measurement bases, we apply an additional layer of $\sqrt{\text{SWAP}}^\dagger$ gates along the y direction, which is a local operations and classical communication inside each chain and cannot enhance entanglement between the two chains. Thus, after these auxiliary gates, we build an observable verifying the interchain entanglement with three measurements. After two measurements, the same as above, we further measure the spin correlation $\sigma_x^1\sigma_y^3\sigma_x^5\sigma_y^7$ by applying a $\pi/2$ pulse with site-dependent phases [28]. Shown in Fig. 4(e), all necessary observables surpass the relevant classical thresholds, leading to the verification of 2D eight-body *full bipartite nonseparability*.

In Fig. 3(c), we can see an approximate reflection symmetry in the measured two-body spin correlations, revealing the symmetry of the target states. The slight spatial-dependent deviations, as in Figs. 3(c) and 3(d), result from the remaining inhomogeneity of the overall trapping potentials and the residual magnetic gradient, which contribute to the infidelity of the generated multipartite entanglement, as observed in Figs. 3(e), 4(b), 4(d), and 4(e). These imperfections can be overcome by optimizing the projected compensation pattern from the DMD and purifying the lattice laser polarization. Besides, the efficiency of 2D spin-resolved detection can be enhanced by a more reliable state-dependent atom transport through upgrading the addressing technique. Such improvements

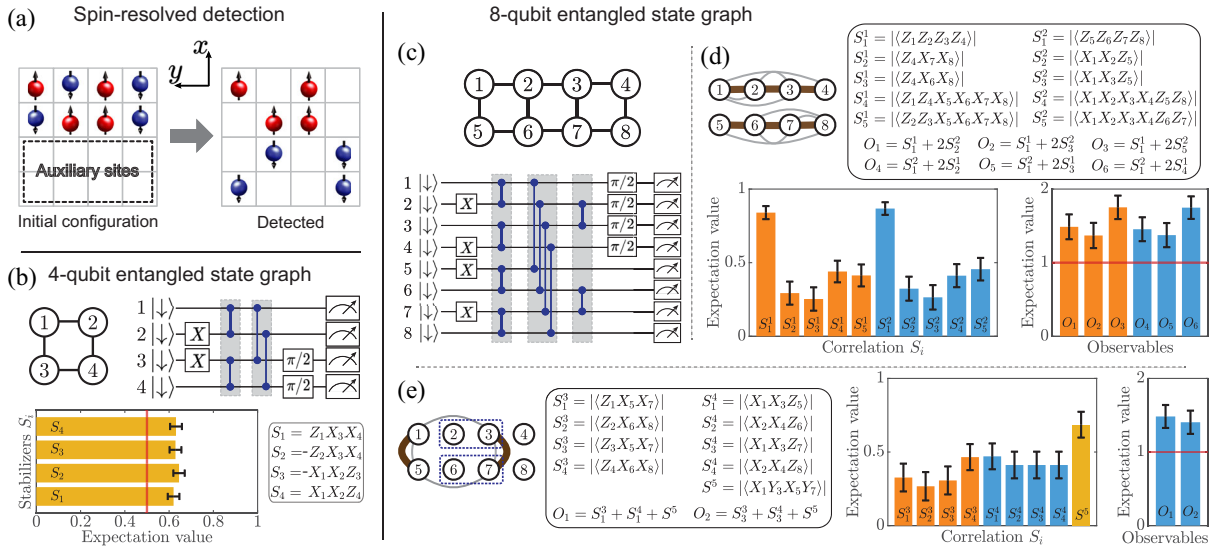

FIG. 4. 2D four-body and eight-body entangled states. (a) A schematic sketch of fully spin-resolved detection in a 2D configuration is achieved via state-dependent atom transport in optical lattices. (b) Top: a 2D, four-body entangled state structure and the corresponding quantum circuit representation of state preparation and measurement. Bottom: measured spin correlations and observables for demonstrating four-body *genuine multipartite entanglement*. (c) Spatial structure of a 2D, eight-body entangled plaquette and the corresponding quantum circuit representation of state preparation and measurement. (d) Measured spin correlations for the first two measurement settings and corresponding observables. These measurements certify the *nonseparability* inside two individual chains, shown with solid brown marks. (e) Measured spin correlations for the last three measurement settings and corresponding observables. These measurements certify the *nonseparability* between the two chains, shown with solid brown marks. All the results presented are not corrected for detection errors. The solid red lines in the histograms represent the threshold for the *full bipartite nonseparability*. Error bars denote the s.e.m.

may allow deep quantum circuits to entangle over hundreds of neutral atoms in a 2D configuration.

Discussion and conclusion.—Our experiments demonstrate the essential ingredients in the roadmap for generating multipartite entangled states with 2-qubit gates, from preparing isolated Bell pairs to realizing 1D entangled chains and 2D entangled plaquettes. High-fidelity quantum circuits are implemented by combining a quantum gas microscope with a cross-angle spin-dependent optical superlattice. For implementing the measurement-based quantum computation (MBQC) [40], our 2-qubit entangling gate can be employed to generate the cluster states with additional single-qubit rotation gates [4,41]. Besides, by integrating versatile, controllable tight-focused optical traps [42,43], we can also perform local measurements and single-qubit gates on individual atoms, satisfying the essential request of MBQC. More generally, our platform can offer new opportunities for exploration in quantum metrology [44], and quantum simulation of intriguing physics in lattice gauge theories [45–49] and exotic quantum phases in the quantum magnetism realm [50]. The capability of realizing low-entropy atom arrays together with the high-precision manipulation of single atoms may open the avenue to demonstrating practical quantum advantage [51].

We thank Otfried Gühne for discussions on entanglement verification, Juan Yin for suggestions on the thermal lensing effect of optics, and Qian Xie, Zhao-Yu Zhou, and Guo-Xian Su for their early contribution to building the experimental setup. This work was supported by the NNSFC Grant No. 12125409, the Innovation Program for Quantum Science and Technology 2021ZD0302000, and the Anhui Initiative in Quantum Information Technologies. H. S. acknowledges support from the National Natural Science Foundation of China, Grant No. 12204469.

[*] These authors contributed equally to this work.

[1] M. A. Nielsen and I. L. Chuang, *Quantum Computation and Quantum Information: 10th Anniversary Edition* (Cambridge University Press, Cambridge, England, 2010).

[2] L. Pezze, A. Smerzi, M. K. Oberthaler, R. Schmied, and P. Treutlein, Quantum metrology with nonclassical states of atomic ensembles, Rev. Mod. Phys. **90**, 035005 (2018).

[3] R. Raussendorf and H. J. Briegel, A One-Way Quantum Computer, Phys. Rev. Lett. **86**, 5188 (2001).

[4] B. Vaucher, A. Nunnenkamp, and D. Jaksch, Creation of resilient entangled states and a resource for measurement-based quantum computation with optical superlattices, New J. Phys. **10**, 023005 (2008).

[5] X.-L. Wang, Y.-H. Luo, H.-L. Huang, M.-C. Chen, Z.-E. Su, C. Liu, C. Chen, W. Li, Y.-Q. Fang, X. Jiang, J. Zhang, L. Li, N.-L. Liu, C.-Y. Lu, and J.-W. Pan, 18-Qubit Entanglement with Six Photons' Three Degrees of Freedom, Phys. Rev. Lett. **120**, 260502 (2018).

[6] M. Gong, M.-C. Chen, Y. Zheng, S. Wang, C. Zha, H. Deng, Z. Yan, H. Rong, Y. Wu, S. Li *et al.*, Genuine 12-Qubit Entanglement on a Superconducting Quantum Processor, Phys. Rev. Lett. **122**, 110501 (2019).
[7] C. Song, K. Xu, H. Li, Y.-R. Zhang, X. Zhang, W. Liu, Q. Guo, Z. Wang, W. Ren, J. Hao *et al.*, Generation of multicomponent atomic Schrödinger cat states of up to 20 qubits, Science **365**, 574 (2019).
[8] Y. Wang, Y. Li, Z.-Q. Yin, and B. Zeng, 16-qubit IBM universal quantum computer can be fully entangled, npj Quantum Inf. **4**, 46 (2018).
[9] G. J. Mooney, G. A. White, C. D. Hill, and L. C. Hollenberg, Generation and verification of 27-qubit Greenberger-Horne-Zeilinger states in a superconducting quantum computer, J. Phys. Commun. **5**, 095004 (2021).
[10] N. Friis, O. Marty, C. Maier, C. Hempel, M. Holzäpfel, P. Jurcevic, M. B. Plenio, M. Huber, C. Roos, R. Blatt *et al.*, Observation of Entangled States of a Fully Controlled 20-Qubit System, Phys. Rev. X **8**, 021012 (2018).
[11] A. Omran, H. Levine, A. Keesling, G. Semeghini, T. T. Wang, S. Ebadi, H. Bernien, A. S. Zibrov, H. Pichler, S. Choi, J. Cui, M. Rossignolo, P. Rembold, S. Montangero, T. Calarco, M. Endres, M. Greiner, V. Vuletić, and M. D. Lukin, Generation and manipulation of Schrödinger cat states in Rydberg atom arrays, Science **365**, 570 (2019).
[12] D. Bluvstein, H. Levine, G. Semeghini, T. T. Wang, S. Ebadi, M. Kalinowski, A. Keesling, N. Maskara, H. Pichler, M. Greiner *et al.*, A quantum processor based on coherent transport of entangled atom arrays, Nature (London) **604**, 451 (2022).
[13] T. Graham, Y. Song, J. Scott, C. Poole, L. Phuttitarn, K. Jooya, P. Eichler, X. Jiang, A. Marra, B. Grinkemeyer *et al.*, Multi-qubit entanglement and algorithms on a neutral-atom quantum computer, Nature (London) **604**, 457 (2022).
[14] D. Jaksch, C. Bruder, J. I. Cirac, C. W. Gardiner, and P. Zoller, Cold Bosonic Atoms in Optical Lattices, Phys. Rev. Lett. **81**, 3108 (1998).
[15] M. Greiner, O. Mandel, T. Esslinger, T. W. Hänsch, and I. Bloch, Quantum phase transition from a superfluid to a Mott insulator in a gas of ultracold atoms, Nature (London) **415**, 39 (2002).
[16] L.-M. Duan, E. Demler, and M. D. Lukin, Controlling Spin Exchange Interactions of Ultracold Atoms in Optical Lattices, Phys. Rev. Lett. **91**, 090402 (2003).
[17] I. Bloch, J. Dalibard, and W. Zwerger, Many-body physics with ultracold gases, Rev. Mod. Phys. **80**, 885 (2008).
[18] S. Trotzky, P. Cheinet, S. Folling, M. Feld, U. Schnorrberger, A. M. Rey, A. Polkovnikov, E. A. Demler, M. D. Lukin, and I. Bloch, Time-resolved observation and control of superexchange interactions with ultracold atoms in optical lattices, Science **319**, 295 (2008).
[19] H.-N. Dai, B. Yang, A. Reingruber, X.-F. Xu, X. Jiang, Y.-A. Chen, Z.-S. Yuan, and J.-W. Pan, Generation and detection of atomic spin entanglement in optical lattices, Nat. Phys. **12**, 783 (2016).
[20] C. S. Chiu, G. Ji, A. Mazurenko, D. Greif, and M. Greiner, Quantum State Engineering of a Hubbard System with Ultracold Fermions, Phys. Rev. Lett. **120**, 243201 (2018).
[21] B. Yang, H. Sun, C.-J. Huang, H.-Y. Wang, Y. Deng, H.-N. Dai, Z.-S. Yuan, and J.-W. Pan, Cooling and entangling ultracold atoms in optical lattices, Science **369**, 550 (2020).
[22] C. Weitenberg, M. Endres, J. F. Sherson, M. Cheneau, P. Schauss, T. Fukuhara, I. Bloch, and S. Kuhr, Single-spin addressing in an atomic Mott insulator, Nature (London) **471**, 319 (2011).
[23] W. S. Bakr, J. I. Gillen, A. Peng, S. Fölling, and M. Greiner, A quantum gas microscope for detecting single atoms in a Hubbard-regime optical lattice, Nature (London) **462**, 74 (2009).
[24] J. F. Sherson, C. Weitenberg, M. Endres, M. Cheneau, I. Bloch, and S. Kuhr, Single-atom-resolved fluorescence imaging of an atomic Mott insulator, Nature (London) **467**, 68 (2010).
[25] C. Gross and W. S. Bakr, Quantum gas microscopy for single atom and spin detection, Nat. Phys. **17**, 1316 (2021).
[26] B. Yang, H.-N. Dai, H. Sun, A. Reingruber, Z.-S. Yuan, and J.-W. Pan, Spin-dependent optical superlattice, Phys. Rev. A **96**, 011602(R) (2017).
[27] P. Zupancic, P. M. Preiss, R. Ma, A. Lukin, M. E. Tai, M. Rispoli, R. Islam, and M. Greiner, Ultra-precise holographic beam shaping for microscopic quantum control, Opt. Express **24**, 13881 (2016).
[28] See Supplemental Material at http://link.aps.org/supplemental/10.1103/PhysRevLett.131.073401 for a detailed description of our experimental procedure, calibrations of various experimental parameters, and theoretical proofs, which includes Refs. [29–32].
[29] R. Ma, M. E. Tai, P. M. Preiss, W. S. Bakr, J. Simon, and M. Greiner, Photon-Assisted Tunneling in a Biased Strongly Correlated Bose Gas, Phys. Rev. Lett. **107**, 095301 (2011).
[30] P. M. Preiss, R. Ma, M. E. Tai, A. Lukin, M. Rispoli, P. Zupancic, Y. Lahini, R. Islam, and M. Greiner, Strongly correlated quantum walks in optical lattices, Science **347**, 1229 (2015).
[31] G. Tóth and O. Gühne, Entanglement detection in the stabilizer formalism, Phys. Rev. A **72**, 022340 (2005).
[32] A. Asadian, P. Erker, M. Huber, and C. Klöckl, Heisenberg-Weyl observables: Bloch vectors in phase space, Phys. Rev. A **94**, 010301 (2016).
[33] M.-D. Li, W. Lin, A. Luo, W.-Y. Zhang, H. Sun, B. Xiao, Y.-G. Zheng, Z.-S. Yuan, and J.-W. Pan, High-powered optical superlattice with robust phase stability for quantum gas microscopy, Opt. Express **29**, 13876 (2021).
[34] M. Boll, T. A. Hilker, G. Salomon, A. Omran, J. Nespolo, L. Pollet, I. Bloch, and C. Gross, Spin-and density-resolved microscopy of antiferromagnetic correlations in Fermi-Hubbard chains, Science **353**, 1257 (2016).
[35] S. Trotzky, Y.-A. Chen, U. Schnorrberger, P. Cheinet, and I. Bloch, Controlling and Detecting Spin Correlations of Ultracold Atoms in Optical Lattices, Phys. Rev. Lett. **105**, 265303 (2010).
[36] Y.-M. Yang, H.-T. Xie, W.-C. Ji, Y.-F. Wang, W.-Y. Zhang, S. Chen, and X. Jiang, Ultra-low noise and high bandwidth bipolar current driver for precise magnetic field control, Rev. Sci. Instrum. **90**, 014701 (2019).
[37] B. Xiao, X.-K. Wang, Y.-G. Zheng, Y.-M. Yang, W.-Y. Zhang, G.-X. Su, M.-D. Li, X. Jiang, and Z.-S. Yuan, Generating two-dimensional quantum gases with high stability, Chin. Phys. B **29**, 076701 (2020).

[38] M.-D. Li, Y.-G. Zheng, W.-Y. Zhang, X.-K. Wang, B. Xiao, Z.-Y. Zhou, L. Jiang, M.-Z. Lian, Z.-S. Yuan, and J.-W. Pan, A high-power and low-noise 532-nm continuous-wave laser for quantum gas microscopy, Rev. Sci. Instrum. **92**, 083202 (2021).

[39] Y. Zhou, B. Xiao, M.-D. Li, Q. Zhao, Z.-S. Yuan, X. Ma, and J.-W. Pan, A scheme to create and verify scalable entanglement in optical lattice, npj Quantum Inf. **8**, 99 (2022).

[40] H. J. Briegel, D. E. Browne, W. Dür, R. Raussendorf, and M. Van den Nest, Measurement-based quantum computation, Nat. Phys. **5**, 19 (2009).

[41] T. Tanamoto, Y.-X. Liu, X. Hu, and F. Nori, Efficient Quantum Circuits for One-Way Quantum Computing, Phys. Rev. Lett. **102**, 100501 (2009).

[42] C. Zhang, S. Rolston, and S. D. Sarma, Manipulation of single neutral atoms in optical lattices, Phys. Rev. A **74**, 042316 (2006).

[43] C. Weitenberg, S. Kuhr, K. Molmer, and J. F. Sherson, Quantum computation architecture using optical tweezers, Phys. Rev. A **84**, 032322 (2011).

[44] Z. Ren, W. Li, A. Smerzi, and M. Gessner, Metrological Detection of Multipartite Entanglement from Young Diagrams, Phys. Rev. Lett. **126**, 080502 (2021).

[45] B. Yang, H. Sun, R. Ott, H.-Y. Wang, T. V. Zache, J. C. Halimeh, Z.-S. Yuan, P. Hauke, and J.-W. Pan, Observation of gauge invariance in a 71-site Bose–Hubbard quantum simulator, Nature (London) **587**, 392 (2020).

[46] Z.-Y. Zhou, G.-X. Su, J. C. Halimeh, R. Ott, H. Sun, P. Hauke, B. Yang, Z.-S. Yuan, J. Berges, and J.-W. Pan, Thermalization dynamics of a gauge theory on a quantum simulator, Science **377**, 311 (2022).

[47] Z. Yao, L. Pan, S. Liu, and H. Zhai, Quantum many-body scars and quantum criticality, Phys. Rev. B **105**, 125123 (2022).

[48] Y. Cheng, S. Liu, W. Zheng, P. Zhang, and H. Zhai, Tunable confinement-deconfinement transition in an ultra-cold atom quantum simulator, PRX Quantum **3**, 040317 (2022).

[49] J. C. Halimeh, I. P. McCulloch, B. Yang, and P. Hauke, Tuning the topological theta-angle in cold-atom quantum simulators of gauge theories, PRX Quantum **3**, 040316 (2022).

[50] A. Bohrdt, L. Homeier, C. Reinmoser, E. Demler, and F. Grusdt, Exploration of doped quantum magnets with ultra-cold atoms, Ann. Phys. (Amsterdam) **435**, 168651 (2021).

[51] A. J. Daley, I. Bloch, C. Kokail, S. Flannigan, N. Pearson, M. Troyer, and P. Zoller, Practical quantum advantage in quantum simulation, Nature (London) **607**, 667 (2022).